iScience

CellPress
OPEN ACCESS

Article

Porous nitrogen-doped reduced graphene oxide-supported CuO@Cu_2O hybrid electrodes for highly sensitive enzyme-free glucose biosensor

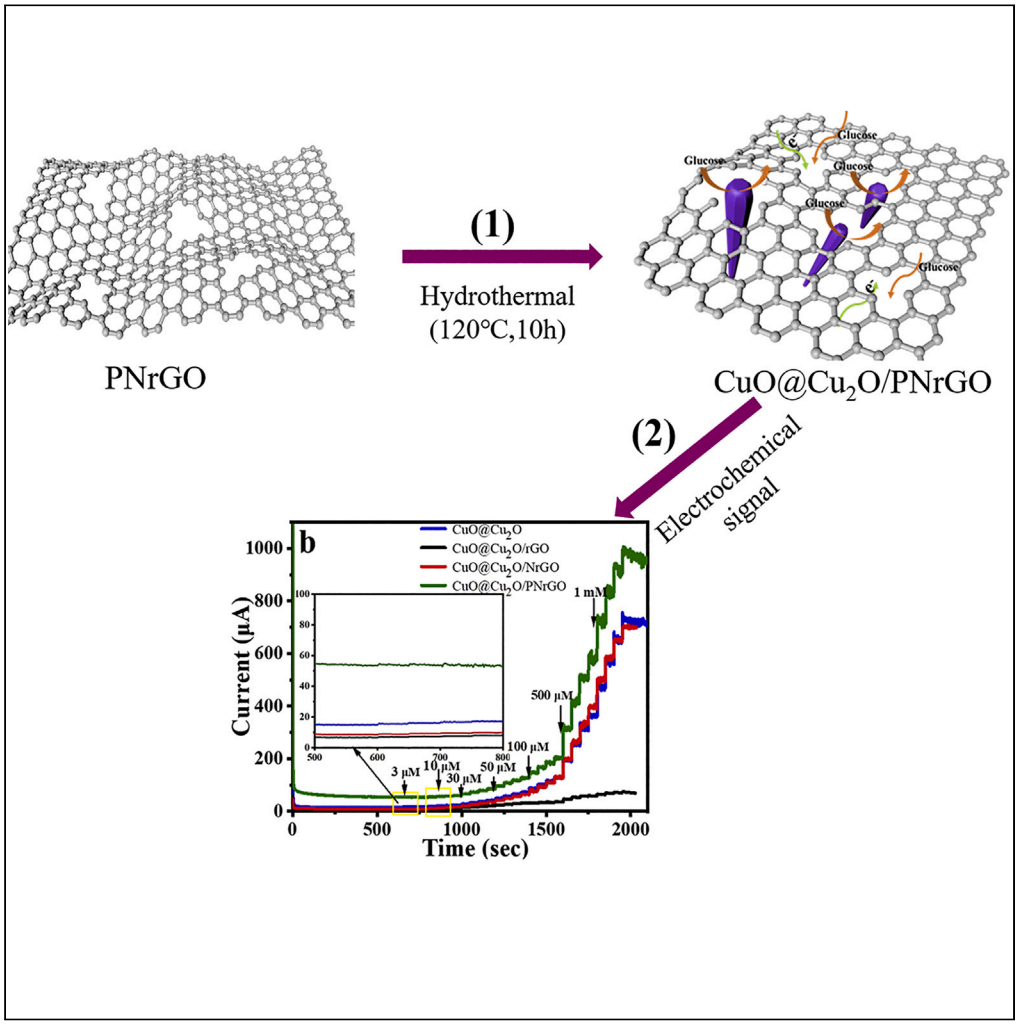

Qing Wei, Ling Wu, Meiwen Zhu, Zhipeng Wang, Zheng-Hong Huang, Ming-Xi Wang

wuling2018@wust.edu.cn (L.W.)
wangzhipeng@jxnu.edu.cn (Z.W.)
wangmx14@wit.edu.cn (M.-X.W.)

Highlights

The as-fabricated biosensor has excellent sensing performance toward glucose

It has multiple high activation sites due to its elaborate structure and composites

The sensor successfully was applied to detect glucose in glucose syrup

The sensor has a wide linear range, low detection limit, and high sensitivity

Wei et al., iScience 26, 106155
March 17, 2023 © 2023
https://doi.org/10.1016/j.isci.2023.106155

iScience

CellPress
OPEN ACCESS

Article

Porous nitrogen-doped reduced graphene oxide-supported CuO@Cu_2O hybrid electrodes for highly sensitive enzyme-free glucose biosensor

Qing Wei,[1] Ling Wu,[2,*] Meiwen Zhu,[3] Zhipeng Wang,[4,*] Zheng-Hong Huang,[5] and Ming-Xi Wang[1,6,*]

SUMMARY

Constructing high-performance enzyme-free biosensors for detecting glucose is essential to preliminary diabetes diagnosis. Here, copper oxide nanoparticles (CuO@Cu_2O NPs) were anchored in porous nitrogen-doped reduced graphene oxide (PNrGO) to construct CuO@Cu_2O/PNrGO/GCE hybrid electrode for sensitive detection of glucose. Benefiting from the remarkable synergistic effects between the multiple high activation sites of CuO@Cu_2O NPs and the dramatic properties of PNrGO with excellent conductivity and large surface area with many accessible pores, the hybrid electrode possesses outstanding glucose sensing performance that is far superior to those of pristine CuO@Cu_2O electrode. The as-fabricated enzyme-free glucose biosensor displays prominent glucose sensitivity of 2,906.07 μA mM^{-1} cm^{-2}, extremely low limit of detection of 0.13 μM, and wide linear detection of 3 μM–6.772 mM. In addition, excellent reproducibility, favorable long-term stability, and distinguished selectivity are obtained in the glucose detection. Importantly, this study provides promising results for continuous improvement of non-enzyme sensing applications.

INTRODUCTION

Diabetes is an awfully chronic disease owing to the higher glucose level than normal in the blood,[1] which can cause numerous complications, for instance, stroke, kidney failure, and heart attack.[2] Consequently, the determination of blood glucose is imperative to fight diabetes, particularly in the initial stage, for the easiest means for diagnosing and prognosticating diabetic patients is the accurate detection of glucose levels. To this end, many glucose sensors have been developed based on various types of transducers, such as optical, acoustic, thermal, magnetic, and electrochemical.[3] Electrochemical sensors have gained ever-increasing attention thanks to their low-cost, efficiency, fast response, and user-friendliness. Electrochemical platforms can be classified into two main categories depending on the presence or absence of enzyme as sensing element. Glucose is quantified by the electron flow, being generated in the glucose oxidation catalyzed by either an enzyme or a substituent material.[1,4] The early electrochemical glucose sensors were based on enzymes, having high accuracy and selectivity. However, they always suffer from poor stability and restricted pH ranges and temperature, due to the biological inactivation of enzymes.[5] Thus, it is necessary to develop enzyme-free glucose sensors with high electrocatalytic activity.

Considerable efforts have been devoted to the exploitation of nanomaterials (NMs) as sensing materials for the catalytic oxidation of glucose,[6] for example, noble metals,[7] transition metals, and metal oxides.[8,9] An ideal NM should have collective properties of high electrocatalytic and enzyme-mimicking activities, but such materials have scarcely been reported. Among these catalysts, transition metal oxides (TMOs) are popular due to their exposed metal active sites with excellent catalytic activity.[10] Copper oxide, a vital member of TMOs, is recognized as a promising catalyst because of its low cost, chemical stability, and abundant active sites. More importantly, the electron transfer reaction could be promoted at lower overpotentials,[11] so copper oxides have been widely used in biosensing and batteries.[12,13] Nevertheless, single TMO NMs (copper oxide nanoparticles [NPs]) tend to agglomerate, resulting in the decrease of their available active sites. In addition, their electronic conductivity is generally poor. So their electrocataltyic activities are not satisfactory, and their sensing performances are also well below expectation.[14] To avoid the spontaneous agglomeration and improve the electronic conductivity, anchoring of copper oxide NPs on a conductive support is an effective strategy, thus promoting their biosensing performance as an

[1]Key Laboratory of Biomass-based Materials for Environment and Energy in Petroleum & Chemical Industries, School of Chemical and Environmental Engineering, Wuhan Institute of Technology, Wuhan 430205, China

[2]Hubei Province Key Laboratory of Coal Conversion and New Carbon Materials, School of Chemistry and Chemical Engineering, Wuhan University of Science and Technology, Wuhan 430081, China

[3]Chongqing Academy of Metrology and Quality Inspection, Chongqing 401123, People's Republic of China

[4]Institute of Advanced Materials, Jiangxi Normal University, 99 Ziyang Avenue, Nanchang 330022, China

[5]Lab of Advanced Materials, School of Materials Science and Engineering, Tsinghua University, Beijing 100084, China

[6]Lead contact

*Correspondence: wuling2018@wust.edu.cn (L.W.), wangzhipeng@jxnu.edu.cn (Z.W.), wangmx14@wit.edu.cn (M.-X.W.)

https://doi.org/10.1016/j.isci.2023.106155

electrochemical sensor. Carbon nanomaterials (CNMs) (i.e., graphene, carbon nanofibers, carbon nanotubes) are outstanding substrate materials for anchoring metal oxide NPs, because they have high surface area, good chemical stability, and excellent electronic conductivity.

Compared with other CNMs, graphene and graphene oxide (GO) have a unique two-dimensional (2D) planar structure, which endows them with much more available surface area for anchoring catalysts.[15,16] In addition, they have high carrier mobility, prominent biocompatibility, and wide potential window, so that the electron transfer rates are greatly facilitated between the active reaction and the electrodes. Thus, they are the desired substrates for anchoring catalysts in biosensor electrodes. Ren et al. constructed an efficient glucose sensor based on the composite electrode of porous nickel on a graphene bottom layer.[17] Besides graphene, reduced graphene oxide (rGO) has been widely employed to construct glucose sensor electrode.[18] Unfortunately, the pristine graphene is readily stacked on top of each other owing to the existence of van der Waals forces and strong π-π stacking between graphene sheets, leading to the reduction of actually available surface area and conductivity, so its electrochemical performance will be deteriorated.[19]

Doping and pore-creating in graphene or GO can not only change notably its semiconducting property[20] but also promote the formation of composite materials with metal NPs. Copper oxide/N-doped rGO (NrGO) nanocomposite was synthesized by a low-temperature aqueous process,[21] displaying excellent oxygen reduction activity. Copper NPs supported on N-doped graphene (NG) was constructed for surface-enhanced Raman scattering.[22] Recently, John et al. prepared modified electrode based on copper nanostructures on NG by electrodeposition toward glucose oxidation,[23] showing higher electrocatalytic activity. The doping of nitrogen can improve the conductivity, spin density, and binding ability of graphene and increase active sites.[24] Creating pores in graphene or GO can effectively increase its surface area, providing more exposed catalytically active sites for anchoring NPs, accordingly reducing the agglomeration of NPs. Moreover, the pores can accommodate more target molecules, promote the full contact between the electrode and electrolyte, and shorten the transmission distance of ions, thus improving the electrocatalytic performance.[25,26]

To the best of our knowledge, there are few studies on nitrogen-doped porous GO-supported copper oxides as enzyme-free glucose sensors.[25,27] Herein, we prepared the nitrogen-doped porous reduced graphene oxide (PNrGO) using a high-temperature calcination method, and used the hydrothermal method to prepare nanocomposites using PNrGO as the support. Electrochemical testing and morphology characterization of nanocomposite materials were systematically investigated. Owing to the synergetic effects between metal oxides and PNrGO, it was found that the hybrid electrode exhibits low detection limits and high sensitivity in the electrochemical detection of glucose.

EXPERIMENTAL SECTION

Figure 1 schematically illustrates the procedures for preparing CuO/Cu_2O anchored on rGO in this study. Initially, GO was synthesized by the modified Hummer's method, and then it was reduced by thermal treatment at 800°C to obtain rGO. NrGO and PNrGO were prepared by mixing GO with urea or urea/KOH followed by heat treatment at 800°C for 3 h. Subsequently, the as-prepared rGO, NrGO, and PNrGO were separately dispersed into ethylene glycol with Cu $(CH_3COO)_2 \cdot H_2O$, H_3COONa under ultrasound for some time; they were then transferred into a 100-mL Teflon-lined stainless-steel autoclave to undergo hydrothermal treatment for 10 h at 120°C and then cooled to room temperature. Finally, the products were rinsed with ethanol and ultrapure water, and CuO/Cu_2O@rGO, CuO/Cu_2O@NrGO, and CuO/Cu_2O@PNrGO were acquired.

The chemicals and experimental details of preparation are given in STAR Methods under sections experimental set-up, as well as the sections preparation of modified electrodes, materials characterizations and electrochemical sensing tests.

RESULTS AND DISCUSSION

Characterization

Morphological examinations

The microstructure and morphology of samples were examined by scanning electron microscopy (SEM) and transmission electron microscopy (TEM). Figures 2A–2C shows the SEM images of pristine rGO,

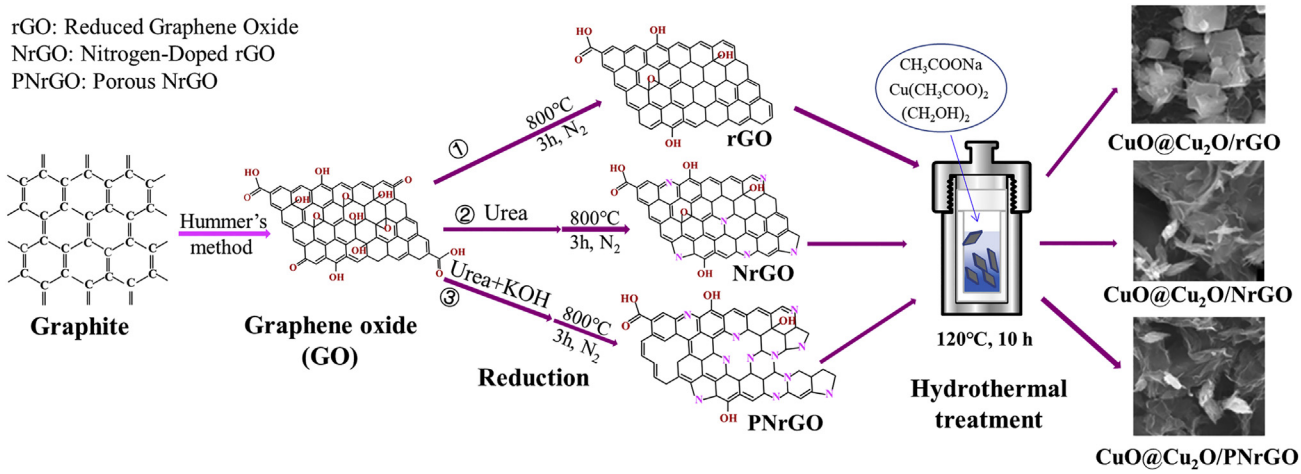

Figure 1. Preparation process of materials

NrGO, and PNrGO. They all exhibit well-exfoliated 2D layered structure with size of less than 100 nm. After nitrogen doping with urea and pore creation by KOH, some wrinkles appeared in NrGO and PNrGO on a larger scale. Figures 2A′–C′ and A″–C″ display the SEM and TEM images of anchoring CuO/Cu_2O on rGO, NrGO, and PNrGO, respectively. It is clearly seen that a lot of metal oxide NPs have been deposited on the substrates. Interestingly, most of the loaded NPs on rGO after hydrothermal treatment appeared as cubic shape, and they usually agglomerated together with larger size as seen in Figure 2A′. By contrast, nearly all the NPs on NrGO and PNrGO in Figures 2B′–C′ were thin shuttle-like structure, and they were evenly dispersed on the surface and in the voids of the graphene sheet. The TEM images in Figures 2A″–2C″ offer a closer look at the distribution of NPs. As shown in Figure 2A″, only a small amount of shuttle-like NPs can be found on rGO with serious agglomeration. On NrGO in Figure 2B″, the NPs are partially agglomerated, indicating that the nitrogen doping into sheets led to good dispersibility of graphene for metal oxide NPs.

With further pore creation in NrGO, the as-obtained PNrGO exhibits more excellent anchoring performance for NPs than the others, for it has larger and more exposed surface as nucleation sites. From Figure 2C″, it is easily found that the NPs became smaller in size and dispersed more uniformly onto PNrGO. To verify this, SEM-EDX (Energy Dispersive X-Ray Spectrometer) mapping analysis was conducted on CuO@Cu_2O/PNrGO. As expected and shown in Figure 2D, there is a uniform distribution of C, O, N, and Cu elements, without other elements on the surface of PNrGO. In addition, Cu element seems to be present around N, which demonstrates that N doping in graphene sheet can act as a binding site for anchoring metal oxides NPs, for it can assist in a stronger coupling between the N-doped carbon and metal oxides.[28] On the contrary, the elements were not distributed well uniformly on the surface of GO, which was confirmed by the SEM-EDX mapping of CuO@Cu_2O/NrGO shown in Figure S1. The colors representing different elements were uneven in Figure S1A, particularly the Cu element, which suggested that Cu distributed in a local area. The high-resolution TEM images of CuO@Cu_2O/PNrGO are profiled in Figure 2E. Well-resolved lattice fringes disclose interplanar distances of 0.27 nm, 0.25 nm, and 0.34 nm, which are in good agreement with the (110), (111), and (002) planes of CuO, Cu_2O, and carbon, confirming the formation of CuO@Cu_2O on PNrGO.

Crystal structure

The phase and crystal structures of the final products were first clarified by XRD. Figure S2 presents the XRD patterns of GO and PNrGO. A sharp diffraction peak at $2\theta = 10.65°$ appeared in the pattern of GO, corresponding to the (002) plane of GO.[29] Compared with GO, PNrGO exhibited a characteristic and broad peak at $2\theta = 24.65°$ due to the disordered stacking of graphene sheets,[25] which demonstrated that GO had been reduced during the preparation process. The XRD patterns of CuO@Cu_2O without or with substrates are shown in Figure 3A. It can be observed that diffraction peaks of CuO and Cu_2O presented in all the samples. The peaks of 2θ around at 32.5°, 35.5°, 38.5°, 48.7°, and 66.1° were ascribed to the (110), (002), (111), (202), and (022) crystal planes of CuO (PDF#89–5895).[30] Significantly, there is only a weak peak for Cu_2O at 61.6° corresponding to its (220) plane in the CuO@Cu_2O-bare, which indicated that the generated metal

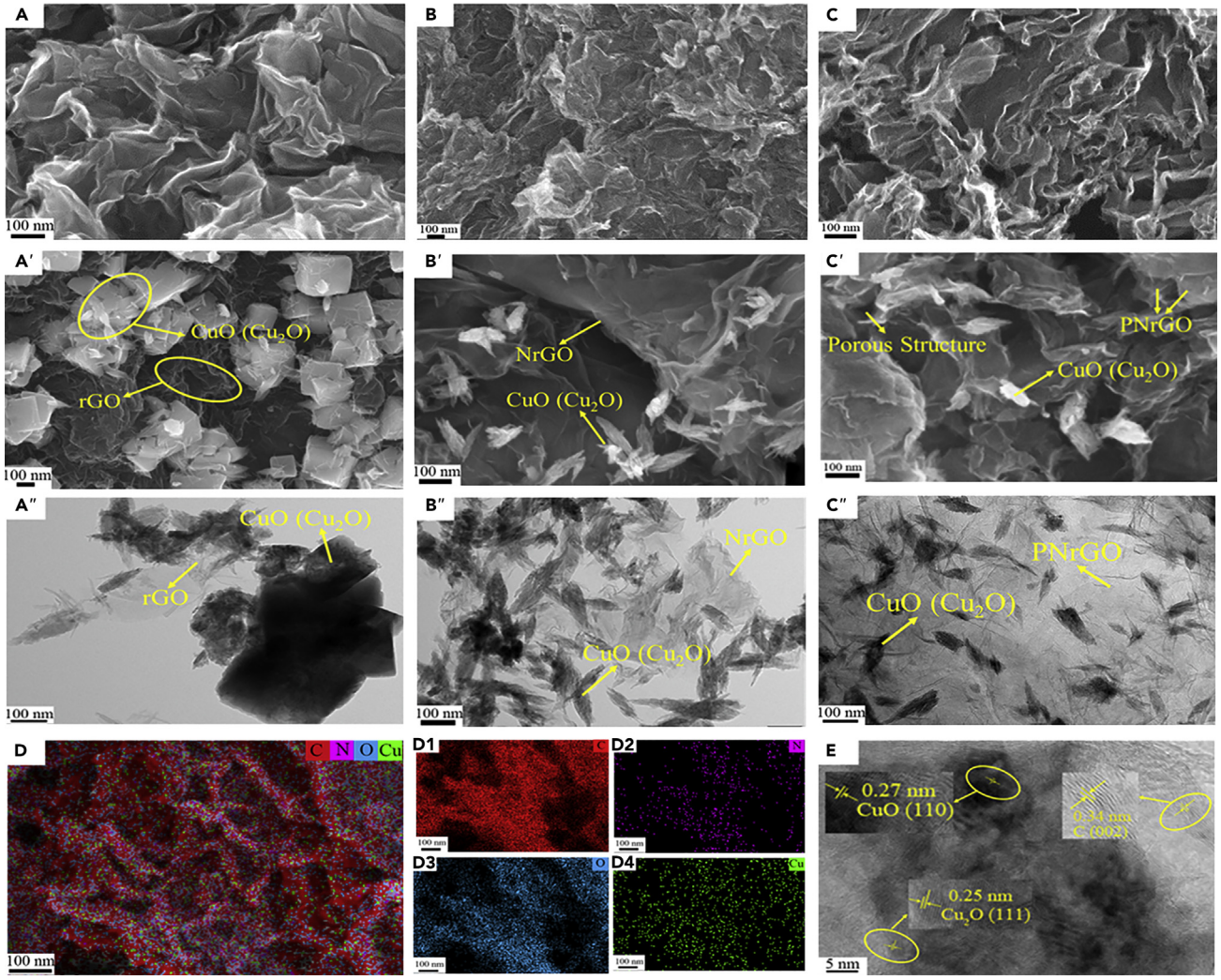

Figure 2. The analysis diagram of morphology and elemental

oxide was mainly CuO in the absence of GO substrate. For the samples in the presence of rGO, NrGO, and PNrGO, not only the carbon peak located around 25° attributed to the typical (002) plane was observed but also another peak of Cu_2O was observed at 43.4° corresponding to the (200) plane of Cu_2O. This fully confirmed that CuO can be partially reduced to Cu_2O, owing to the strong reduction action of rGO, NrGO, and PNrGO under hydrothermal treatment.

Their crystalline natures were further confirmed by Raman spectroscopy, a powerful means for the identification of GO and its nanohybrids as well as different oxides. Figure 3B shows the Raman spectra of rGO, NrGO, and PNrGO. All have two wide bands centered at 1,354 and 1,595 cm^{-1}; these bands can be deconvoluted into I, D, D″, and G bands.[31,32] Among these bands, D represents the in-plane and edge defects, and G originates from the graphitic carbon domain formed by sp^2-hybridized carbon, so the intensity ratio of D to G band (I_D/I_G) is a reliable index to reflect the degree of structural defects.[33] The values of I_D/I_G and other fitting parameters including the bands center (ν, cm^{-1}) and full width at half maximum (Γ, cm^{-1}) are summarized in Table S1. The values of I_D/I_G increased from 1.59 (rGO) to 1.66 (NrGO) and 1.68 (PNrGO), which implied that doping nitrogen and pore creation reduced the degree of graphitization resulting in the generation of more defects in the graphene sheets. The increased defect is beneficial to the anchoring metal oxide NPs and the improvement of the sensing performance. The Raman spectra of CuO@Cu_2O/rGO nanohybrids were also recorded in the range of 160–2,000 cm^{-1} and shown in Figure 3B′. In the measured Raman spectra of bare CuO@Cu_2O and hybrid CuO@Cu_2O/PNrGO, three bands were

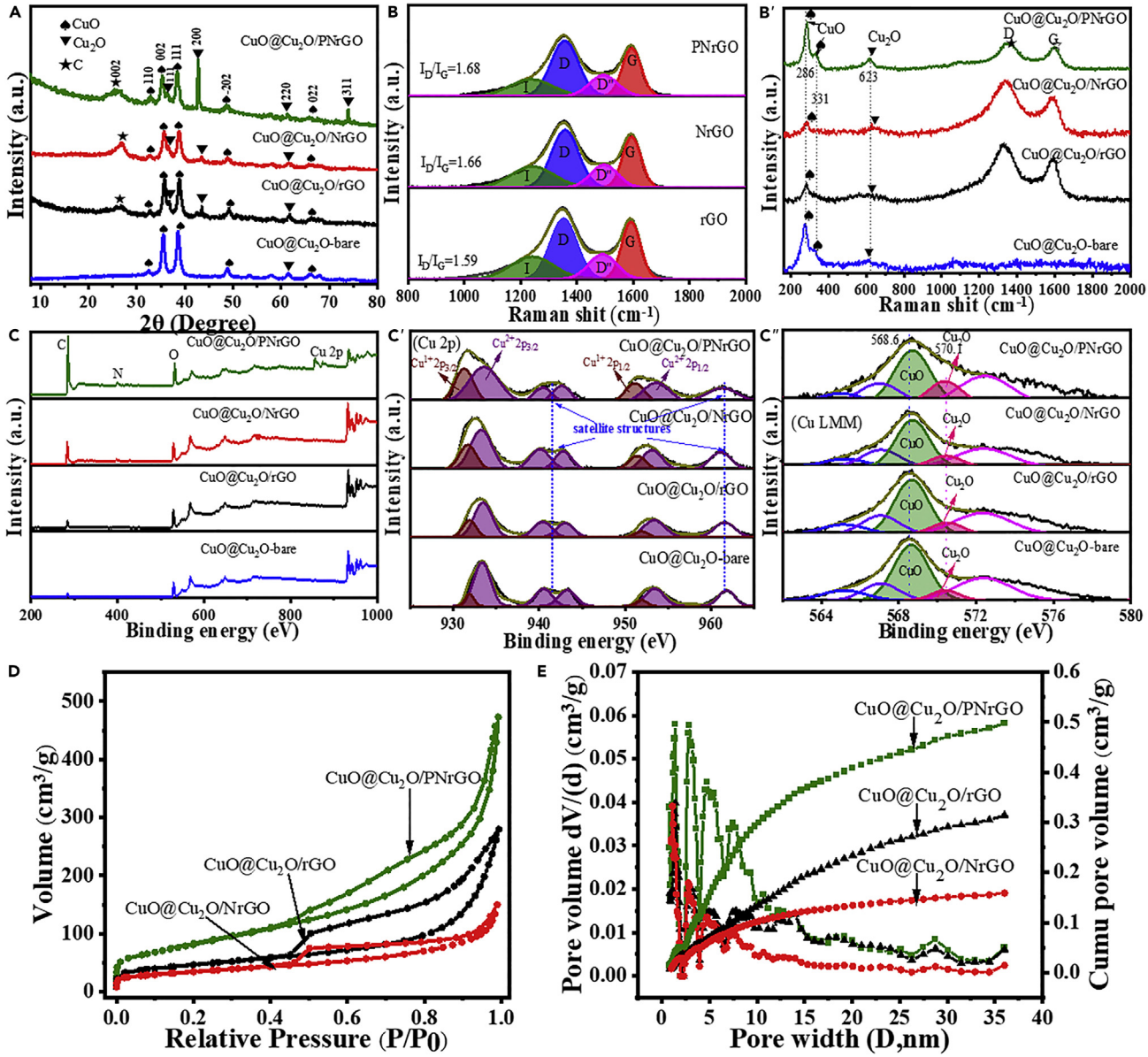

Figure 3. Characterization of structure and composition of materials

(A) XRD patterns.

(B, B′) Raman spectra.

(C–C″) Survey, high-resolution XPS. spectra of Cu 2p and Cu LMM AES spectra.

(D) Nitrogen adsorption-desorption isotherms. (E) Pore size distribution curves of samples.

observed, such as the relatively strong band at 286 cm^{-1} and other two weak bands at 331 and 623 cm^{-1}, which can be assigned to the CuO and Cu_2O components,[34,35] respectively. In the spectra of hybrid CuO@Cu_2O/rGO and CuO@Cu_2O/NrGO, there was only one obvious band at 286 cm^{-1}. Of course, the characteristic bands of GO including D and G bands appeared in all the hybrids except the CuO@Cu_2O-bare. This reveals that PNrGO is the most excellent substrate for anchoring metal oxide NPs, and is helpful for the enhancement of its sensing performance.

Compositional analysis

X-ray photoelectron spectroscopy (XPS) measurements were performed on CuO@Cu_2O/rGO hybrids to gain insight into the composition and chemical state of elements. From the survey of XPS spectra in

Figure 3C, N 1s peak at 398 eV was only observed in the spectra of CuO@Cu_2O/NrGO and CuO@Cu_2O/PNrGO; C 1s, O 1s, and Cu 2p peaks can be found in all the samples. N species comes from the urea, and the N 1s spectra shown in Figure S5 can be split into four peaks centered at 398.1, 399.6, 401.1, and 402.6 eV, which are attributed to the pyridinic-N, pyrrolic/pyridone-N, graphitic-N, and N-oxide,[36,37] respectively. For CuO@Cu_2O-bare and CuO@Cu_2O/rGO, no N 1s spectrum was found due to the absence of nitrogen source during hydrothermal treatment. The high-resolution C 1s spectra were displayed in Figure S6, which can be deconvlouted into three peaks located at 284.45, 285.62, and 288.25 eV, corresponding to the sp^2C-C, C-O/C=N, and O-C=O functional groups.[31,38]

The high-resolution spectra of Cu 2p and Cu LMM spectra are given in Figure 3C′–C″. The Cu 2p XPS spectra exhibit two main Cu $2p_{3/2}$ and Cu $2p_{1/2}$ peaks together with two shake-up satellite peaks for all the samples.[39] Obviously, the centers of Cu $2p_{3/2}$ and Cu $2p_{1/2}$ peaks' binding energy were shifted toward left from CuO@Cu_2O-bare to CuO@ Cu_2O/PNrGO, which was caused by their compositional change. In fact, the peaks are composed of Cu^+ and Cu^{2+} and can be further fitted. The dominant peaks with shoulder located at 933.3 and 953.4 eV are ascribed to Cu^{2+}, whereas the weak peaks at 931.8 and 951.9 eV may arise from Cu^+ or Cu^0 after reduction for their nearly same binding energy.[40] To distinguish them, Cu LMM AES (Auger electron spectroscopy) spectrum was employed and is displayed in Figure 3C″. In the peak fit of Cu LMM, there is a strong peak centered at 568.6 eV and four other weak peaks at 565.2, 567.1, 570.1, and 573.1 eV. It is well-recognized that the characteristic Auger peaks of Cu^0, Cu^+, and Cu^{2+} are centered at 568.0, 570.0, and 568.6 eV,[41] respectively. Combining with the XRD, Raman data, and Cu 2p analysis results as well as the preparation conditions, it can be concluded that copper species existed in the form of CuO and Cu_2O in all the samples. According to the fitted results listed in Table S2, the intensity of Cu_2O/CuO peaks grew continuously from CuO@Cu_2O-bare to CuO@Cu_2O/rGO, CuO@Cu_2O/NrGO, and CuO@Cu_2O/PNrGO. This demonstrates that Cu_2O was readily produced under the reduction role of the substrate to form Cu_2O@CuO hybrid metal oxides, which are beneficial to the enhancement of glucose electrochemical sensing.

Textural analysis

Furthermore, textural analysis of CuO@Cu_2O hybrids was conducted to identify their textures. Figures 3D and 3E present the nitrogen adsorption-desorption isotherms and pore size distributions (PSDs). Seen from Figure 3D, an obvious hysteresis loop exists in all the isotherms, suggesting the presence of mesopores.[38,42] In addition, the nitrogen uptake follows the order CuO@Cu_2O/rGO < CuO@Cu_2O/NrGO < CuO@Cu_2O/PNrGO. Their PSDs are plotted in Figure 3E and the calculated textural parameters are listed in Table S3, which confirmed the presence of mesopores and the order of their specific surface area (SSA) and pore volume. CuO@Cu_2O/rGO has an SSA of 164 m^2/g and pore volume of 0.314 cm^3/g, which is greater than those of CuO@Cu_2O/NrGO of 120 m^2/g and 0.159 cm^3/g yet lower than those of CuO@Cu_2O/PNrGO of 294 m^2/g and 0.498 cm^3/g. The decrease of SSA for NrGO is due to the nitrogen resource (urea), which may restrict the thermal expansion of GO during the hydrothermal treatment and lead to the formation of curvature structure of NrGO as depicted in SEM images.[43] The increase of SSA for CuO@Cu_2O/PNrGO originates from the pore creation of KOH, which would react violently with the carbon substrate to produce a large number micropores and mesopores.

Electrochemical sensing test

Electrocatalytic characteristics of the modified electrodes

Glucose was electrochemically detected using the CuO@Cu_2O-based modified electrodes, whose catalytic activities have extremely important influence on their performance for glucose detection. Figure 4A shows the Nyquist plots of different modified electrodes; the insets are the equivalent circuit and list of calculated resistances. The open-circuit voltage was first determined by open circuit potential-time, and those of CuO@Cu_2O, CuO@Cu_2O/rGO, CuO@Cu_2O/NrGO, and CuO@Cu_2O/PNrGO were 0.39, 0.419, 0.404, and 0.375 V, respectively. Then the electrochemical impedance spectroscopy (EIS) test is performed with perturbation amplitude of 5 mV over a frequency range of 1–10^6 Hz. Finally, we use Zview software to fit the data to calculate R_{ct}. All the electrodes exhibited close solution resistance (R_s) of approximately 11 Ω, for they were measured in the same electrolyte. Nevertheless, there exists evident difference in the charge transfer resistance (R_{ct}) among them. The bare CuO@Cu_2O had a relatively great R_{ct} of 99.42 Ω. After it was anchored on the substrates of rGO, NrGO, and PNrGO, the R_{ct} of hybrid electrodes decreased to 85.31, 87.25, and 80.17 Ω, respectively. The reduction in R_{ct} can be ascribed to the substrate (rGOs), which greatly improves the conductivity of bare CuO@Cu_2O. Notably, CuO@Cu_2O/PNrGO/GCE (glass carbon

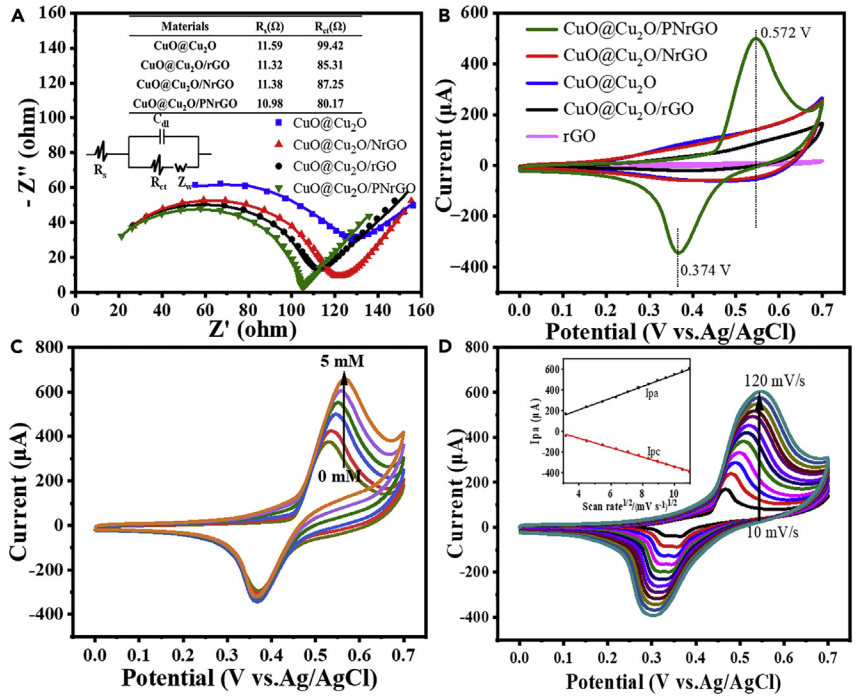

Figure 4. Electrochemical characterization and cyclic voltammetry curves

(A) Nyquist plots of EIS for different modified electrodes in KCl solution containing 5 mM $[Fe(CN)_6]^{3-/4-}$.

(B) Cyclic voltammogram (CV) in 0.1 M NaOH + 2 mM glucose at a scan rate of 50 mV/s.

(C) CV curves of CuO@Cu_2O/PNrGO in different concentrations from 0 to 5 mM glucose.

(D) CV of CuO@Cu_2O/PNrGO/GCE in 0.1 M NaOH solution (2 mM glucose) with different scanning rates, (inset: linear relationship between the peak current and scan rates).

electrode) possesses the lowest R_{ct}, because it has the highest active surface area when compared with other electrodes.

As displayed in Figure 4B, the cyclic votammogram (CV) curves of all electrodes were compared with 0.1 M NaOH containing 2 mM glucose. The CV curve of rGO/GCE presented almost a straight line, implying no response to the glucose detection due to the absence of electrocatalytic activity. The CuO@Cu_2O/rGO/GCE exhibited a certain amount of current in 0.1 M NaOH with glucose, whereas the CuO@Cu_2O/GCE and CuO@Cu_2O/NrGO/GCE have nearly the same and higher current. Surprisingly, the CV curve of CuO@Cu_2O/PNrGO/GCE exhibited not only much greater current than those of other electrodes but also remarkable redox peaks located at 0.374 and 0.572 V. Moreover, the redox peaks were very sharp, indicating that strong glucose oxidation occurred over the CuO@Cu_2O/NrGO/GCE electrode. The appearance of obvious redox peaks was ascribed to the significantly increased SSA and the synergistic effects between CuO@Cu_2O and PNrGO, for it can provide larger SSA and more active sites for glucose oxidation. According to the previous studies, the overall kinetics of glucose oxidation is not sufficient to generate enough faradaic currents over metal surface.[44] In addition, the faradaic currents are proportional to the apparent area of the electrode, and they are very sensitive to the nanoscopic surface area.[45] As discussed above, the SSA of CuO@Cu_2O/PNrGO was improved dramatically and the substrate (PNrGO) was conductive graphene nanosheets.

To further investigate the electrochemical behavior of CuO@Cu_2O/PNrGO/GCE, we adjusted the glucose concentration from 0 to 5 mM, and the CV curves were obtained as shown in Figure 4C. With the increase of glucose concentration, the oxidation peak current increased, indicating that CuO@Cu_2O/PNrGO/GCE has electrocatalytic effect on glucose oxidation. The redox peak pair observed in 0.1 M NaOH solution is attributed to the transition reaction between Cu^{3+} and Cu^{2+} (Cu^{1+})[8,46,47]; Cu^{2+} (Cu^{1+}) loses electrons in an alkaline environment to become Cu^{3+} (Cu^{2+}) as shown in Equations 1 and 2. In the presence of glucose, the metal ions (Cu^{3+} or Cu^{2+}) with a high oxidation state oxidize glucose to gluconolactone (Equations 3

and 4), which generates a significant electrical signal on the electrode, increasing the peak oxidation current compared with the peak oxidation current in 0.1 M NaOH solution. Therefore, the redox pair peaks were ascribed to both the $Cu^{3+/}Cu^{2+}(Cu^{+})$ redox reaction in NaOH and the glucose oxidation.

$$Cu^{1+}+OH^{-}\rightarrow Cu^{2+}+e^{-} \quad \text{(Equation 1)}$$

$$Cu^{2+}+OH^{-}\rightarrow Cu^{3+}+e^{-} \quad \text{(Equation 2)}$$

$$Cu^{3+}+e^{-}+\text{Glucose}\rightarrow Cu^{2+}+OH^{-}+\text{Gluconolactone} \quad \text{(Equation 3)}$$

$$Cu^{2+}+e^{-}+\text{Glucose}\rightarrow Cu^{1+}+OH^{-}+\text{Gluconolactone} \quad \text{(Equation 4)}$$

Moreover, the CV curves in 0.1 M NaOH with 2 mM glucose were measured at different scanning rates and displayed in Figure 4D. With the increase of scanning rate, the currents of redox (oxidation and reduction) peaks increased and the peak potentials shifted, because high scan rate requires a greater electrochemical reaction rate that is faster than the diffusion speed of the electrolyte in a redox reaction, thus leading to the appearance of polarization and the shift of redox peaks.[48] The relationship between the peak current and the scan rate is plotted and shown in the inset in Figure 4D to explore the electrocatalytic kinetics of glucose. It can be clearly seen that the peak current of oxidation and reduction is well linearly related to the square root of the scanning rate, and the current versus scanning rate follows the equations: $I_{pa}(\mu A) = 56.42\upsilon^{1/2}(mV^{1/2}s^{-1/2})-15.99(R^2 = 0.9989)$ and $I_{pc}(\mu A) = -45.73\upsilon^{1/2}(mV^{1/2}s^{-1/2})+117.2$ ($R^2 = 0.9962$), indicating that the electrocatalytic oxidation process of glucose belongs to diffusion control.

Furthermore, the sensing performance of $CuO@Cu_2O$/PNrGO/GCE for glucose in phosphate buffer solution (PBS) (0.1 M, PH = 7.4) was investigated; Figure S7A shows the CV curves with various concentrations of glucose from 0 to 4 mM. Consistent with the results in NaOH solution, the response current gradually increased with the increase of glucose concentration; the linear relationship between the current and concentration is displayed in Figure S7B. By contrast, the current value in PBS was much lower than that in NaOH and the redox peaks is inconspicuous. The calculated sensitivity and detection limit in PBS were 53.65 $\mu A\ mM^{-1}\ cm^{-2}$ and 0.27 mM, whereas the G-PANI(COOH)-PEI-Fc/Cu-MCNB/GCE[49] and CuO/graphene electrodes[50] had sensitivity of 14.3 and 37.62 $\mu A\ mM^{-1}cm^{-2}$ and detection limit of 0.16 and 5.04 mM, respectively. It is clear that the as-prepared $CuO@Cu_2O$/PNrGO/GCE exhibited more excellent performance in PBS than the previously reported sensors.

Optimization of detection conditions

The testing conditions usually have prominent influence on the glucose detection results, so they should be optimized. Figures 5A–A′ show the effect of amount of active electrode materials on the detection signal. The concentrations of NaOH (C_{NaOH}), glucose, and electrode materials were controlled at 0.1 M, 2 mM, and 2 mg/mL, respectively. From the CV curves of $CuO@Cu_2O$/PNrGO/GCE in Figure 5A, it can be seen that the signal strength increased with the increase of suspension volume from 1 to 6 μL, whereas it decreased as the suspension volume was increased to 7 and 8 μL. For other electrode materials, including $CuO@Cu_2O$, $CuO@Cu_2O$/rGO, and $CuO@Cu_2O$/NrGO, similar results were measured and shown in Figure 5A′. The maximal anodic peak current was obtained at suspension volume of 6 μL for all the electrodes. This can be explained as follows: too few active electrode materials cannot provide enough active sites for the electrocatalysis of glucose, but excess materials will increase the resistance of ion transfer. So the optimal amount was selected as 6 μL.

Figures 5B and B′ show the effect of C_{NaOH} on the detection signal strength; the C_{NaOH} varied from 0.001 to 0.2 M. The detection signal also first increased then decreased with increase of C_{NaOH}, and the maximal signal was achieved when C_{NaOH} was 0.1 M, for too high C_{NaOH} may easily deteriorate glucose to form 5-hydroxymethylfurfural.[51] Interestingly, whether under any suspension volume or C_{NaOH}, the signal strength with $CuO@Cu_2O$/PNrGO/GCE was far greater than those with the other modified

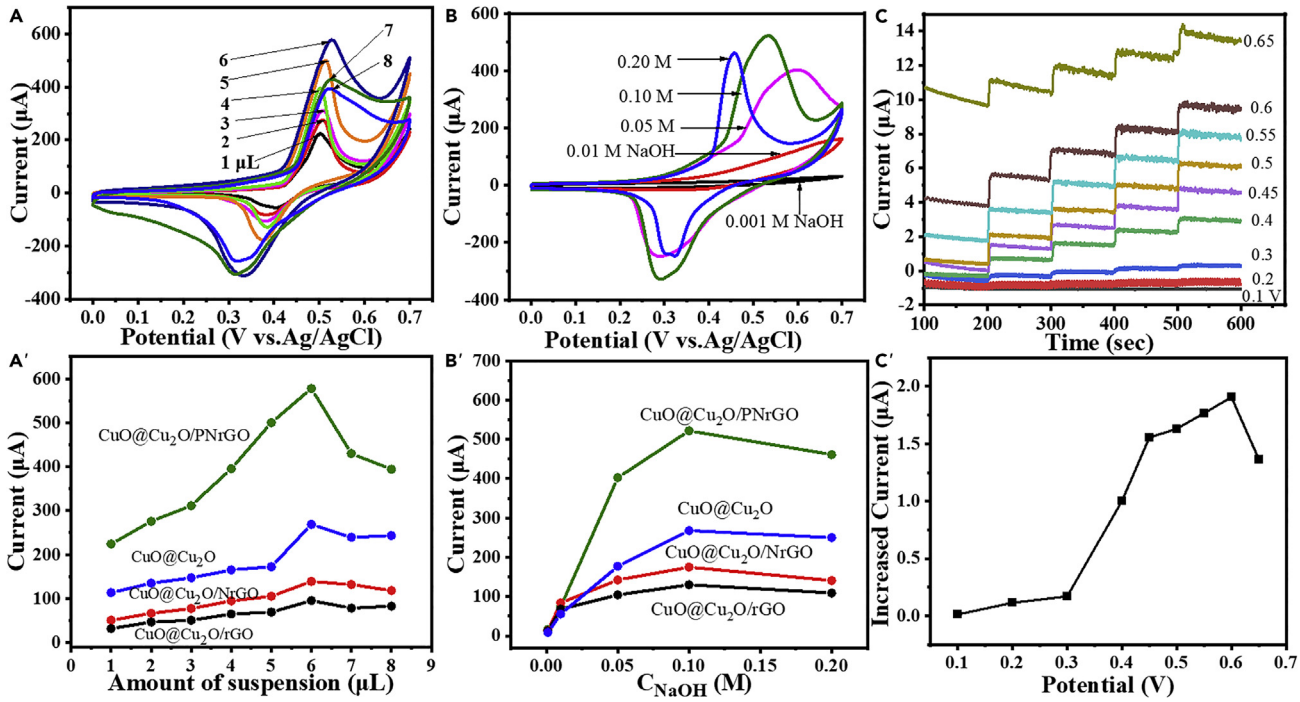

Figure 5. Optimization of electrochemical test conditions

(A) CV curves of $CuO@Cu_2O$@PNrGO/GCE with suspension volume.

(A′) Anodic peak currents versus suspension volume of all electrode materials.

(B) CV curves of $CuO@Cu_2O$@PNrGO/GCE under different NaOH concentrations.

(B′) Anodic peak currents versus NaOH concentrations for all the electrodes.

(C) Amperometric response at the applied potential.

(C′) The plots of amperometric response current versus applied positive potential.

electrodes, which verified again that $CuO@Cu_2O$/PNrGO was the most outstanding electrochemical sensor material for glucose detection. Besides C_{NaOH}, the applied potential is crucial for acquiring sensible amperometric response in the glucose detection, so it is optimized by chronoamperometry performed at different potentials with successive addition of glucose over $CuO@Cu_2O$/PNrGO/GCE. Seen from Figures 5C and C′, the responsive current increased steadily with the increase of the applied potential from 0.10 to 0.60 V, for higher potential is conducive to the formation of more active species carrying charges of glucose oxidation.[48] On the other hand, when the applied potential rose to 0.65 V, the responsive current displayed decrease instead of increase deviating from the linearity; the maximum current was observed at 0.60 V. This is because overhigh applied potential will induce the occurrence of oxygen evolution and decrease of active surface,[5] resulting in elevated current background and lower current response. Especially, as the applied potential arrived at 0.70 V as shown in Figure S8, the background current increased dramatically, whereas the responsive current was almost negligible. Therefore, the optimal applied potential was chosen as 0.6 V with optimal suspension volume of 6 μL and C_{NaOH} of 0.1 M in the subsequent tests.

Sensing performance for glucose detection

Under optimal testing conditions, the electrochemical responses of $CuO@Cu_2O$/rGOs/GCE biosensors were scrutinized toward glucose with successive addition and different concentrations. As displayed in Figure 6A, except for the pristine rGO-based sensors, the other $CuO@Cu_2O$-based biosensors generated prompt amperometric responses within short response time, and gradually increasing steady-state currents were produced with every 30 μM glucose added. Moreover, the corresponding response of $CuO@Cu_2O$/PNrGO/GCE is significantly higher than those of $CuO@Cu_2O$/NrGO/GCE, $CuO@Cu_2O$/GCE, and $CuO@Cu_2O$/rGO/GCE, which agrees well with the CV results (Figure 4B). $CuO@Cu_2O$/PNrGO/GCE is the optimal biosensor, in which $CuO@Cu_2O$ is anchored on the PNrGO nanosheets, demonstrating the most outstanding electrocatalytic activity of the nanocomposite toward glucose oxidation.

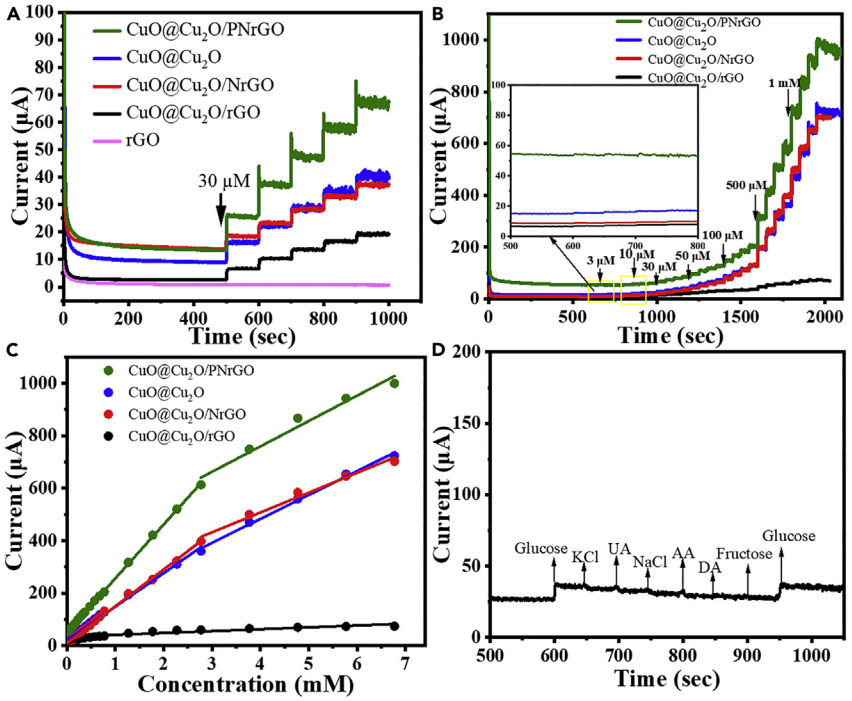

Figure 6. Amperometric current responses of the modified electrodes to 0.1 M NaOH

(A) With successive addition of 30 μM glucose.

(B) Different concentrations of glucose.

(C) Plots of response current versus the various concentrations of glucose.

(D) Interference tests of CuO@Cu_2O/PNrGO/GCE: amperometric responses with addition of 50 μM glucose, 5 μM of the following interfering species (KCl, uric acid [UA], NaCl, ascorbic acid [AA], and dopamine [DA]), and 50 μM glucose.

The quantitative ranges of the CuO@Cu_2O-based sensors were assessed by amperometry. The real-time amperometric response curves and the corresponding linear fit curves are exhibited in Figures 6B and 6C, respectively. With the successive addition of different glucose concentrations from 3 μM to 1 mM into a stirred 0.1 M NaOH solution, the current reached a steady state within extremely short time. After stabilizing for some time, an increased concentration of glucose was added every 50 s, the modified electrodes presented a fast response to the change of glucose concentration, in that the response current immediately enhanced and attained the steady state. This indicated that the biosensor possessed a fast electrocatalytic current response to glucose electrooxidation. The observation of the amplitude of current enhancement revealed that the electrocatalytic activity followed the order CuO@Cu_2O/PNrGO/GCE > CuO@Cu_2O/GCE ≈ CuO@Cu_2O/NrGO/GCE > CuO@Cu_2O/rGO/GCE. As shown in the linear fit curves (Figure 6C), the catalytic current of glucose oxidation with its concentration was observed to present two linear ranges except for the CuO@Cu_2O/rGO/GCE. The linear range, sensitivity, and detection limit are summarized in Table S4. The detection limit is calculated according to the 3S/N (signal-to-noise ratio) using the error bar. It can be found that the sensitivity of CuO@Cu_2O/PNrGO/GCE is 2,906.07 μA mM^{-1} cm^{-2} and 1,370.08 μA mM^{-1} cm^{-2} within the linear range of 0.0003–2.772 and 2.772–6.772 mM, respectively, which is remarkably better than those of other electrodes. Furthermore, the detection limit of CuO@Cu_2O/PNrGO/GCE is 0.13 μM, which is also much lower than those of other electrodes. The detection performances of the fabricated modified electrodes were compared with those of some other copper oxide-based enzyme-free glucose sensors listed in Table S4. It is clear that the CuO@Cu_2O/PNrGO/GCE modified electrode has the lowest detection limit, highest sensitivity, and widest linear range.

In addition to the detection limit, sensitivity and linear range, the selectivity, reproducibility, and stability are important criteria to appraise glucose biosensors in practical applications. Particularly, the selectivity of biosensor is of essence, for some electrochemical oxidation signals may derive from interfering species. Normally, many biomolecules with redox properties coexist with glucose in human blood, such as uric acid, ascorbic

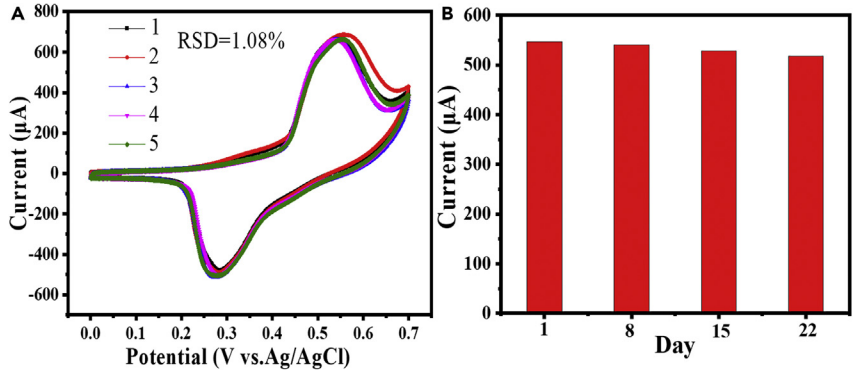

Figure 7. The test of reproducibility and stability

(A) The reproducibility test of CuO@Cu_2O/PNrGO/GCE in 2 mM glucose solution.

(B) The stability test of CuO@Cu_2O/PNrGO/GCE in 2 mM glucose solution.

acid, fructose, and dopamine. Besides, some common ions like K^+, Na^+, and Cl^- can also affect the glucose quantification, and Cl^- can poison the biosensor resulting in loss of sensing activity. Therefore, the selectivity of the as-fabricated CuO@Cu_2O/PNrGO/GCE biosensor was examined against oxygen in 0.1 M NaOH solution. As depicted in Figure 6D, there is hardly any conspicuous current fluctuation with the addition of 5 μM of any interfering species, whereas a strong current step can still be produced with the further addition of 50 μM glucose. Figure S9 shows the percentage of interference signals when compared with glucose, which clearly indicates that the response current of the interfering substance is almost negligible compared with that of glucose. The amperometeric response results confirm that the CuO@Cu_2O/PNrGO biosensor has an excellent anti-interference ability and significant selectivity for glucose detection.

To investigate the reproducibility and stability of the proposed biosensor, different CuO@Cu_2O/PNrGO biosensors were fabricated in the same procedure and scanned by CV in 2 mM glucose with 0.1 M NaOH standard solution under the same conditions. The typical CV curves of all five electrodes in Figure 7A clearly show that the CuO@Cu_2O/PNrGO biosensor has excellent reproducibility, for the change in these CVs is almost negligible and the relative SD(RSD) of the oxidation peak current was only 1.08% (n = 5). Then, the biosensor was stored at room temperature in air for 3 weeks without additional use. During this period, its stability was evaluated every 7 days in 2 mM glucose solution with four consecutive tests. As displayed in Figure 7B, the oxidation current of glucose decreased slightly to 94.8% of the initial state after 3 weeks, confirming that the proposed biosensor has superb storage stability for glucose detection. Finally, the practical application of the biosensor was also examined by detecting the commercial glucose syrup. The purchased glucose syrup was diluted with 0.1 M NaOH solution, and the concentration was analyzed by the standard addition method. As listed in Table S5, the recoveries of glucose measured by the modified electrode were 96.4%–97.8%, and the RSD was less than 5%, indicating that the accurate quantitative analysis of glucose can be applied to the actual sample analysis.

Based on the above results, the CuO@Cu_2O/PNrGO-based biosensor showed optimal sensing performance in glucose detection, which is mainly ascribed to the abundant porosity and nitrogen dopant of PNrGO. On one hand, creating pores in rGO can effectively increase its SSA and pore volume confirmed by the nitrogen adsorption-desorption isotherms, providing more exposed fixation sites for metal oxides thereby reducing the agglomeration of metal oxides verified by the SEM and TEM images. On the other hand, higher porosity can accommodate more target molecules and promote the full contact between the electrode and electrolyte, shortening the transmission distance of ions. Thus, the electrochemical sensing performance of the CuO@Cu_2O/PNrGO-based biosensor was greatly improved.

Conclusion

Here, we presented a highly efficient enzyme-free glucose biosensor based on CuO@Cu_2O-PNrGO hybrid electrode, in which CuO@Cu_2O NPs were dispersedly anchored on porous NrGO nanosheets. The biosensor shows superb sensing performance for glucose detection, such as high sensitivity, outstanding selectivity, and extremely low detection limit and response time. In real serum analysis, the developed biosensor also exhibited satisfied precision and accuracy in determining glucose concentration. The

superior electrocatalytical oxidation toward glucose of CuO@Cu_2O/PNrGO originates from rapid electron transfer thanks to the synergistic effects between copper oxide NPs and porous NrGO. The as-fabricated CuO@Cu_2O/PNrGO has high SSA, porosity, abundant exposed active sites, and nitrogen element. The porous structure of nitrogen-doped GOs provide more nucleation sites for the metal oxide reducing the occurrence of agglomeration and improving the conductivity of the metal oxide, and ensure sufficient contact between the reactant and active site shortening the transmission distance of ions and promoting the progress of the catalytic reaction. Therefore, CuO@Cu_2O/PNrGO hybrid electrode exhibited prominent electrochemical sensing performance for glucose detection.

Limitations of the study

The performance of the 0.1 M NaOH solution is higher than that of the buffer solution with pH = 7, which may cause some problems in the measurement of blood glucose in practical applications (for example, the plasma needs to be placed in a strongly alkaline solution to measure glucose content). Future research will focus on the development of NMs as electrochemical sensing materials that can determine glucose content at near-neutral pH conditions.

STAR★METHODS

Detailed methods are provided in the online version of this paper and include the following:

SUPPLEMENTAL INFORMATION

Supplemental information can be found online at https://doi.org/10.1016/j.isci.2023.106155.

ACKNOWLEDGMENTS

The work was financially supported by the Fund of National Natural Science Foundation of China (No. 21802105, No. 51872130, and No. 52063016), Research Fund of Hubei Provincial Department of Education (No. D20211102), and the Innovation Project of Key Laboratory of Novel Biomass-based Environmental and Energy Materials in Petroleum and Chemical Industry (22BEEA05).

AUTHOR CONTRIBUTIONS

Q.W.: constructed experimental plan, completed material synthesis and electrochemical test. L.W.: completed the material morphology characterization and analysis. M.Z.: contributed to the general methodology and reviewed the manuscript. Z.W.: conducted physicochemical characterization and analysis of the synthesized materials and reviewed the manuscript. Z.-H.H.: supervise the process from idea generation to final paper writing. M.-X.W.: supervised experiments, writing – review and editing, and funding acquisition. All authors contributed to the article and approved the submitted version.

DECLARATION OF INTERESTS

The authors declare no competing interests.

Received: January 17, 2023
Revised: January 30, 2023
Accepted: February 3, 2023
Published: February 8, 2023

REFERENCES

1. Adeel, M., Rahman, M.M., Caligiuri, I., Canzonieri, V., Rizzolio, F., and Daniele, S. (2020). Recent advances of electrochemical and optical enzyme-free glucose sensors operating at physiological conditions. Biosens. Bioelectron. *165*, 112331–112343. https://doi.org/10.1016/j.bios.2020.112331.

2. Hu, Y., Jiang, X., Zhang, L., Fan, J., and Wu, W. (2013). Construction of near-infrared photonic crystal glucose-sensing materials for ratiometric sensing of glucose in tears. Biosens. Bioelectron. *48*, 94–99. https://doi.org/10.1016/j.bios.2013.03.082.

3. Niu, X., Li, X., Pan, J., He, Y., Qiu, F., and Yan, Y. (2016). Recent advances in non-enzymatic electrochemical glucose sensors based on non-precious transition metal materials: opportunities and challenges. RSC Adv. *6*, 84893–84905. https://doi.org/10.1039/c6ra12506a.

4. Grieshaber, D., MacKenzie, R., Vörös, J., and Reimhult, E. (2008). Electrochemical biosensors-sensor principles and architectures. Sensors *8*, 1400–1458. https://doi.org/10.3390/s80314000.

5. Gao, A., Zhang, X., Peng, X., Wu, H., Bai, L., Jin, W., Wu, G., Hang, R., and Chu, P.K. (2016). In situ synthesis of $Ni(OH)_2/TiO_2$ composite film on NiTi alloy for non-enzymatic glucose sensing. Sensor. Actuator. B Chem. *232*, 150–157. https://doi.org/10.1016/j.snb.2016.03.122.

6. Sehit, E., and Altintas, Z. (2020). Significance of nanomaterials in electrochemical glucose sensors: an updated review (2016-2020). Biosens. Bioelectron. *159*, 112165–112182. https://doi.org/10.1016/j.bios.2020.112165.

7. Jia, H., Chang, G., Lei, M., He, H., Liu, X., Shu, H., Xia, T., Su, J., and He, Y. (2016). Platinum nanoparticles decorated dendrite-like gold nanostructure on glassy carbon electrodes for enhancing electrocatalysis performance to glucose oxidation. Appl. Surf. Sci. *384*, 58–64. https://doi.org/10.1016/j.apsusc.2016.05.020.

8. Liu, W., Chai, G., Zhao, X., Dai, Y., and Qi, Y. (2020). Effect of different copper sources on the morphology of cuprous oxide and its application as a non-enzymatic glucose sensor. Sensor. Actuator. B Chem. *321*, 128485–128495. https://doi.org/10.1016/j.snb.2020.128485.

9. Zhou, Q., Zhang, Y., Zeng, T., Wan, Q., and Yang, N. (2021). Morphology-dependent sensing performance of CuO nanomaterials. Anal. Chim. Acta *1171*, 338663. https://doi.org/10.1016/j.aca.2021.338663.

10. Xu, J., Li, F., Wang, D., Nawaz, M.H., An, Q., Han, D., and Niu, L. (2019). Co_3O_4 nanostructures on flexible carbon cloth for crystal plane effect of nonenzymatic electrocatalysis for glucose. Biosens. Bioelectron. *123*, 25–29. https://doi.org/10.1016/j.bios.2018.07.039.

11. Yang, S., Li, G., Wang, D., Qiao, Z., and Qu, L. (2017). Synthesis of nanoneedle-like copper oxide on N-doped reduced graphene oxide: a three-dimensional hybrid for nonenzymatic glucose sensor. Sensor. Actuator. B Chem. *238*, 588–595. https://doi.org/10.1016/j.snb.2016.07.105.

12. Liu, X., Yang, W., Chen, L., and Jia, J. (2017). Three-dimensional copper foam supported CuO nanowire arrays: an efficient non-enzymatic glucose sensor. Electrochim. Acta *235*, 519–526. https://doi.org/10.1016/j.electacta.2017.03.150.

13. Meng, J., Yang, Z., Chen, L., Qin, H., Cui, F., Jiang, Y., and Zeng, X. (2020). Energy storage performance of CuO as a cathode material for aqueous zinc ion battery. Mater. Today Energy *15*, 100370–100377. https://doi.org/10.1016/j.mtener.2019.100370.

14. Chen, A., Ding, Y., Yang, Z., and Yang, S. (2015). Constructing heterostructure on highly roughened caterpillar-like gold nanotubes with cuprous oxide grains for ultrasensitive and stable nonenzymatic glucose sensor. Biosens. Bioelectron. *74*, 967–973. https://doi.org/10.1016/j.bios.2015.07.074.

15. Ojha, R.P., Lemieux, P.A., Dixon, P.K., Liu, A.J., and Durian, D.J. (2004). Statistical mechanics of a gas-fluidized particle. Nature *427*, 521–523. https://doi.org/10.1038/nature02294.

16. Peigney, A., Laurent, C., Flahaut, E., Bacsa, R., and Rousset, A. (2001). Specific surface area of carbon nanotubes and bundles of carbon nanotubes. Carbon *39*, 507–514. https://doi.org/10.1016/s0008-6223(00)00155-x.

17. Ren, Z., Mao, H., Luo, H., and Liu, Y. (2019). Glucose sensor based on porous Ni by using a graphene bottom layer combined with a Ni middle layer. Carbon *149*, 609–617. https://doi.org/10.1016/j.carbon.2019.04.073.

18. Matysiak-Brynda, E., Sęk, J.P., Kasprzak, A., Królikowska, A., Donten, M., Patrzalek, M., Poplawska, M., and Nowicka, A.M. (2019). Reduced graphene oxide doping with nanometer-sized ferrocene moieties–New active material for glucose redox sensors. Biosens. Bioelectron. *128*, 23–31. https://doi.org/10.1016/j.bios.2018.12.037.

19. Wu, K.L., Jiang, B.B., Cai, Y.M., Wei, X.W., Li, X.Z., and Cheong, W.C. (2017). Efficient electrocatalyst for glucose and ethanol based on Cu/Ni/N-doped graphene hybrids. Chemelectrochem *4*, 1419–1428. https://doi.org/10.1002/celc.201700078.

20. Zhao, Y., Hu, C., Hu, Y., Cheng, H., Shi, G., and Qu, L. (2012). A versatile, ultralight, nitrogen-doped graphene framework. Angew. Chem., Int. Ed. Engl. *51*, 11371–11375. https://doi.org/10.1002/anie.201206554.

21. Zhou, R., Zheng, Y., Hulicova-Jurcakova, D., and Qiao, S.Z. (2013). Enhanced electrochemical catalytic activity by copper oxide grown on nitrogen-doped reduced graphene oxide. J. Mater. Chem. *1*, 13179–13185. https://doi.org/10.1039/c3ta13299d.

22. Zhang, X., Shi, C., Liu, E., Li, J., Zhao, N., and He, C. (2015). Nitrogen-doped graphene network supported copper nanoparticles encapsulated with graphene shells for surface-enhanced Raman scattering. Nanoscale *7*, 17079–17087. https://doi.org/10.1039/c5nr04259c.

23. Gowthaman, N.S.K., Raj, M.A., and John, S.A. (2017). Nitrogen-doped graphene as a robust scaffold for the homogeneous deposition of copper nanostructures: a nonenzymatic disposable glucose sensor. ACS Sustain. Chem. Eng. *5*, 1648–1658. https://doi.org/10.1021/acssuschemeng.6b02390.

24. Rahsepar, M., Foroughi, F., and Kim, H. (2019). A new enzyme-free biosensor based on nitrogen-doped graphene with high sensing performance for electrochemical detection of glucose at biological pH value. Sensor. Actuator. B Chem. *282*, 322–330. https://doi.org/10.1016/j.snb.2018.11.078.

25. Zhao, Y., Bo, X., and Guo, L. (2015). Highly exposed copper oxide supported on three-dimensional porous reduced graphene oxide for non-enzymatic detection of glucose. Electrochim. Acta *176*, 1272–1279. https://doi.org/10.1016/j.electacta.2015.07.143.

26. Zhang, Y., Wan, Q., and Yang, N. (2019). Recent advances of porous graphene: synthesis, functionalization, and electrochemical applications. Small *15*, e1903780–e1903818. https://doi.org/10.1002/smll.201903780.

27. Yang, J., Tan, W., Chen, C., Tao, Y., Qin, Y., and Kong, Y. (2017). Nonenzymatic glucose sensing by CuO nanoparticles decorated nitrogen-doped graphene aerogel. Mater. Sci. Eng. C Mater. Biol. Appl. *78*, 210–217. https://doi.org/10.1016/j.msec.2017.04.097.

28. Liang, Y., Li, Y., Wang, H., Zhou, J., Wang, J., Regier, T., and Dai, H. (2011). Co_3O_4 nanocrystals on graphene as a synergistic catalyst for oxygen reduction reaction. Nat. Mater. *10*, 780–786. https://doi.org/10.1038/nmat3087.

29. Zhang, Y., Liu, Y.Q., Bai, Y., Chu, W., and Sh, J. (2020). Confinement preparation of hierarchical NiO-N-doped carbon@ reduced

graphene oxide microspheres for high-performance non-enzymatic detection of glucose. Sensor. Actuator. B Chem. *309*, 127779–127814. https://doi.org/10.1016/j.snb.2020.127779.

30. Liu, X., Cui, S., Qian, M., Sun, Z., and Du, P. (2016). In situ generated highly active copper oxide catalysts for the oxygen evolution reaction at low overpotential in alkaline solutions. Chem. Commun. *52*, 5546–5549. https://doi.org/10.1039/c6cc00526h.

31. He, D., Gao, Y., Wang, Z., Yao, Y., Wu, L., Zhang, J., Huang, Z.H., and Wang, M.X. (2021). One-step green fabrication of hierarchically porous hollow carbon nanospheres (HCNSs) from raw biomass: formation mechanisms and supercapacitor applications. J. Colloid Interface Sci. *581*, 238–250. https://doi.org/10.1016/j.jcis.2020.07.118.

32. Ye, X., Wu, L., Zhu, M., Wang, Z., Huang, Z.H., and Wang, M.X. (2022). Lotus pollen-derived hierarchically porous carbons with exceptional adsorption performance toward reactive black 5: isotherms, kinetics and thermodynamics investigations. Separ. Purif. Technol. *300*, 121899–121913. https://doi.org/10.1016/j.seppur.2022.121899.

33. He, D., Wu, L., Wang, Z., Huang, Z.H., and Wang, M.X. (2021). Hierarchically porous carbons with diverse microstructures derived from crude oil via "One-for-All" strategy. Carbon *184*, 340–345. https://doi.org/10.1016/j.carbon.2021.08.039.

34. Mu, S., Lu, H., Wu, Q., Li, L., Zhao, R., Long, C., and Cui, C. (2022). Hydroxyl radicals dominate reoxidation of oxide-derived Cu in electrochemical CO_2 reduction. Nat. Commun. *13*, 3694–3698. https://doi.org/10.1038/s41467-022-31498-8.

35. Dubale, A.A., Tamirat, A.G., Chen, H.M., Berhe, T.A., Pan, C.J., Su, W.N., and Hwang, B.J. (2016). A highly stable CuS and CuS–Pt modified Cu_2O/CuO heterostructure as an efficient photocathode for the hydrogen evolution reaction. J. Mater. Chem. A Mater. *4*, 2205–2216. https://doi.org/10.1039/c5ta09464j.

36. Gao, Y., He, D., Wu, L., Wang, Z., Yao, Y., Huang, Z.H., Yang, H., and Wang, M.X. (2021). Porous and ultrafine nitrogen-doped carbon nanofibers from bacterial cellulose with superior adsorption capacity for adsorption removal of low-concentration 4-chlorophenol. Chem. Eng. J. *420*, 127411–127427. https://doi.org/10.1016/j.cej.2020.127411.

37. Xu, M., Wu, L., Zhu, M., Wang, Z., Huang, Z.H., and Wang, M.X. (2022). Self-supporting nitrogen-doped reduced graphene oxide@carbon nanofiber hybrid membranes as high-performance integrated air cathodes in microbial fuel cells. Carbon *193*, 242–257. https://doi.org/10.1016/j.carbon.2022.03.024.

38. He, D., Wu, L., Yao, Y., Zhang, J., Huang, Z.H., and Wang, M.X. (2020). A facile route to high nitrogen-containing porous carbon fiber sheets from biomass-flax for high-performance flexible supercapacitors. Appl. Surf. Sci. *507*, 145108–145119. https://doi.org/10.1016/j.apsusc.2019.145108.

39. Mao, Y., He, J., Sun, X., Li, W., Lu, X., Gan, J., Liu, Z., Gong, L., Chen, J., Liu, P., and Tong, Y. (2012). Electrochemical synthesis of hierarchical Cu_2O stars with enhanced photoelectrochemical properties. Electrochim. Acta *62*, 1–7. https://doi.org/10.1016/j.electacta.2011.10.106.

40. Kim, J.Y., Hong, D., Lee, J.C., Kim, H.G., Lee, S., Shin, S., Kim, B., Lee, H., Kim, M., Oh, J., et al. (2021). Quasi-graphitic carbon shell-induced Cu confinement promotes electrocatalytic CO_2 reduction toward C_{2+} products. Nat. Commun. *12*, 3765–3775. https://doi.org/10.1038/s41467-021-24105-9.

41. Wang, Y., Zhou, W., Jia, R., Yu, Y., and Zhang, B. (2020). Unveiling the activity origin of a copper-based electrocatalyst for selective nitrate reduction to ammonia. Angew. Chem., Int. Ed. Engl. *59*, 5350–5354. https://doi.org/10.1002/anie.201915992.

42. Li, C., He, D., Huang, Z.H., and Wang, M.X. (2018). Hierarchical micro-/mesoporous carbon derived from rice husk by hydrothermal pre-treatment for high performance supercapacitor. J. Electrochem. Soc. *165*, A3334–A3341. https://doi.org/10.1149/2.0121814jes.

43. Li, D., Duan, X., Sun, H., Kang, J., Zhang, H., Tade, M.O., and Wang, S. (2017). Facile synthesis of nitrogen-doped graphene via low-temperature pyrolysis: the effects of precursors and annealing ambience on metal-free catalytic oxidation. Carbon *115*, 649–658. https://doi.org/10.1016/j.carbon.2017.01.058.

44. Liu, Y., Liu, S., Chen, R., Zhan, W., Ni, H., and Liang, F. (2015). An antibacterial nonenzymatic glucose sensor composed of carbon nanotubes decorated with silver nanoparticles. Electroanalysis *27*, 1138–1143. https://doi.org/10.1002/elan.201400568.

45. Park, S., Chung, T.D., and Kim, H.C. (2003). Nonenzymatic glucose detection using mesoporous platinum. Anal. Chem. *75*, 3046–3049. https://doi.org/10.1021/ac0263465.

46. Lin, L.-Y., Karakocak, B.B., Kavadiya, S., Soundappan, T., and Biswas, P. (2018). A highly sensitive non-enzymatic glucose sensor based on Cu/Cu_2O/CuO ternary composite hollow spheres prepared in a furnace aerosol reactor. Sensor. Actuator. B Chem. *259*, 745–752. https://doi.org/10.1016/j.snb.2017.12.035.

47. Wu, L., Lu, Z., and Ye, J. (2019). Enzyme-free glucose sensor based on layer-by-layer electrodeposition of multilayer films of multi-walled carbon nanotubes and Cu-based metal framework modified glassy carbon electrode. Biosens. Bioelectron. *135*, 45–49. https://doi.org/10.1016/j.bios.2019.03.064.

48. Zhang, L., Ding, Y., Li, R., Ye, C., Zhao, G., and Wang, Y. (2017). Ni-Based metal–organic framework derived Ni@ C nanosheets on a Ni foam substrate as a supersensitive non-enzymatic glucose sensor. J. Mater. Chem. B *5*, 5549–5555. https://doi.org/10.1039/c7tb01363a.

49. Gopalan, A.I., Muthuchamy, N., Komathi, S., and Lee, K.P. (2016). A novel multicomponent redox polymer nanobead based high performance non-enzymatic glucose sensor. Biosens. Bioelectron. *84*, 53–63. https://doi.org/10.1016/j.bios.2015.10.079.

50. Foroughi, F., Rahsepar, M., Hadianfard, M.J., and Kim, H. (2017). Microwave-assisted synthesis of graphene modified CuO nanoparticles for voltammetric enzyme-free sensing of glucose at biological pH values. Mikrochim. Acta *185*, 57. https://doi.org/10.1007/s00604-017-2558-8.

51. Combs, E., Cinlar, B., Pagan-Torres, Y., Dumesic, J.A., and Shanks, B.H. (2013). Influence of alkali and alkaline earth metal salts on glucose conversion to 5-hydroxymethylfurfural in an aqueous system. Catal. Commun. *30*, 1–4. https://doi.org/10.1016/j.catcom.2012.10.011.

STAR★METHODS

KEY RESOURCES TABLE

REAGENT or RESOURCE	SOURCE	IDENTIFIER
Chemicals, peptides, and recombinant proteins		
D (+)-Glucose	Sinopharm Chemical Reagent Co., Ltd	N/A
N, N-Dimethylformamidel	Sinopharm Chemical Reagent Co., Ltd	N/A
NaCl	Sinopharm Chemical Reagent Co., Ltd	N/A
L-Ascorbic acid	Sinopharm Chemical Reagent Co., Ltd	N/A
Ethylene glycol	Sinopharm Chemical Reagent Co., Ltd	N/A
$KMnO_4$	Sinopharm Chemical Reagent Co., Ltd	N/A
Cu $(CH_3COO)_2 \cdot H_2O$	Tianjin Fu chen Chemical Reagent	N/A
NaOH	Xi long science Co., Ltd	N/A
KOH	Xi long science Co., Ltd	N/A
Urea	Xi long science Co., Ltd	N/A
KCl	Xi long science Co., Ltd	N/A
H_3COONa	Xi long science Co., Ltd	N/A
H_3PO_4	Sinopharm Chemical Reagent Co., Ltd	N/A
H_2SO_4	Sinopharm Chemical Reagent Co., Ltd	N/A
H_2O_2	Sinopharm Chemical Reagent Co., Ltd	N/A
HCl	Sinopharm Chemical Reagent Co., Ltd	N/A
Uric acid	Energy Chemical	N/A
Dopamine hydrochloride	Energy Chemical	N/A
Other		
Electrochemical workstation	CHI760E	N/A
High precision analytical balance	AUW220D	N/A
Tube furnace	GSL-1600X	N/A
Freeze-dryer	FD-1A-50	N/A
Thermostatic water bath	HH	N/A
Air blast drying oven		N/A
vacuum drying oven	DZF-6020	N/A
Field emission scanning electron microscope	Geminisem 300	N/A
Transmission Electron Microscopy	JEOL 2100F	N/A
Raman spectra	Ram HR800 Raman spectrometer	N/A
X-ray diffraction	Bruker D8 Advances 25	N/A
X-ray photoelectron spectra	Thermo Scientific ESCALAB Xi+	N/A
Nitrogen adsorption and desorption isotherms	ASAP 2460	N/A

RESOURCE AVAILABILITY

Lead contact

Further information and requests should be directed to and will be fulfilled by the lead contacts, Ming-Xi Wang (Wangmx14@wit.edu.cn).

Materials availability

This study did not generate new unique reagents.

Additional information

Any additional information required to reanalyze the data reported in this paper is available from the lead contact upon request.

Data and code availability

- Data reported in this paper will be shared by the lead contacts upon reasonable request.
- This study does not report any original code.
- Any additional information required to reanalyze the data reported in this paper is available from the lead contacts upon reasonable request.

EXPERIMENTAL MODEL AND SUBJECT DETAILS

This study does not use experimental models.

METHOD DETAILS

Chemicals

D (+)-Glucose, N, N-Dimethylformamidel, NaCl, L-Ascorbic acid, Ethylene glycol, ethanol, H_3PO_4, H_2SO_4, HCl, H_2O_2 and $KMnO_4$ were purchased from Sinopharm Chemical Reagent Co., Ltd. KOH, NaOH, Urea, KCl, H_3COONa were purchased from Xi long science Co., Ltd. Cu $(CH_3COO)_2 \cdot H_2O$ was purchased from Tianjin Fu chen Chemical Reagent. Uric acid (UA), Dopamine hydrochloride (DA) were purchased from Energy Chemical.

Experimental set-up

All electrochemical tests were performed on a CHI760E electrochemical workstation (Shanghai Chenhua). High precision analytical balance type AUW220D. GSL-1600X tube furnace from Hefei Kejing Co., LTD. The model FD-1A-50 freeze-dryer is manufactured in Jiangsu Tianling Instrument Co., LTD. Thermostatic water bath made in Changzhou Guoyu Instrument Manufacturing Co., LTD. Air blast drying oven produced in Shanghai Langxuan Experimental Equipment Co., LTD. DZF-6020 vacuum drying oven is produced in Shanghai Heng Scientific Instrument Co., LTD.

Materials characterizations

The morphologies of the material were observed using a field emission scanning electron microscope (FESEM, Geminisem 300). Transmission Electron Microscopy (TEM) images were obtained on JEOL 2100F with Ultrascan CCD. X-ray diffraction (XRD) measurements were carried out in Bruker D8 Advances 25, the patterns were achieved in the 2θ range from 8 to 80° with Cu Ka (λ = 1.54 Å). The X-ray photoelectron spectra (XPS) were recorded on Thermo Scientific ESCALAB Xi + to evaluate the compositions of the nanocomposites and the valence of copper in the samples. Raman spectra were measured by Lab Ram HR800 Raman spectrometer. Nitrgoen adsorption-desorption isotherms were achieved at 77 K on an ASAP 2460 (Micromeritics, USA). Specific surface area (SSA) was calculated by Brunauer-Emmet-Teller (BET) model, and the pore volume and pore size distributions (PSDs) were deduced according to the Non-Local Density Functional Theory (NLDFT) model assuming the slit pore in carbon samples.

Chemical synthesis

Preparation of graphene: Typically, 1.5 g graphite powder, 180 mL concentrated H_2SO_4 (98 wt %) and 20 mL concentrated H_3PO_4 were mixed in a beaker, 1.5 g $KMnO_4$ was slowly added while stirring in an ice water bath. After intensive mixing, the mixture was heated to 50°C within water bath and stirred for 12 h, obtaining dark green suspension. The above suspension was added with ice and magnetic stirring. During the stirring process, 30% H_2O_2 was added dropwise using a rubber-tip dropper until the solution turns light yellow. They were washed using firstly HCl followed by centrifugation, then washed with distilled water until the pH value is neutral. Finally, the products were dried by vacuum freeze-dry for 3 days and stored for later use.

Preparation of rGO, NrGO and PNrGO: 0.5 g GO, 2.5 g urea and 1 g KOH were dissolved in a certain amount of distilled water, and then magnetically stirred for 1h. Pour the above solution into a crucible and dry at 80°C. Place it in a tube furnace at 800°C for 3h with N_2, centrifuge and wash until it is neutral

and dry. Compared with PNrGO, NrGO is prepared without adding KOH as a pore-forming agent, and rGO is prepared without adding urea and potassium hydroxide, and other preparation methods are the same.

Preparation of $CuO@Cu_2O$, $CuO@Cu_2O$/rGO, $CuO@Cu_2O$/NrGO and $CuO@Cu_2O$/PNrGO: 0.05 g Cu $(CH3COO)_2 \cdot H_2O$, 0.041 g H_3COONa and 0.02 g PNrGO were dissolved in a certain amount of ethylene glycol and sonicated for 40 min, and then the uniform suspension was poured into the reactor at 120°C for 10 h. Centrifuge washing with ethanol and deionized water and vacuum drying at 60°C. $CuO@Cu_2O$/NrGO and $CuO@Cu_2O$/rGO were prepared by NrGO and rGO instead of PNrGO, respectively. The other preparation procedures were the same.

Preparation of modified electrodes

2 mg of the prepared nanocomposite including $CuO@Cu_2O$, $CuO@Cu_2O$/rGO, $CuO@Cu_2O$/NrGO and $CuO@Cu_2O$/PNrGO were dissolved in 1 mL DMF and sonicated for 30 min to form 2 mg/mL suspension. The bare GCE (3 mm in diameter) was polished with 0.1 μm, 0.3 μm, and 0.05 μm polished aluminum powders, respectively, and then the electrodes were repeatedly rinsed with absolute ethanol and deionized water. Finally, the prepared dispersion was transferred to the electrodes (When the influence of the amount of drip coating on the catalytic performance of the material was studied, 1,2,3,4,5,6 μL were applied respectively.).

Electrochemical sensing test

All electrochemical tests were performed on a CHI760E electrochemical workstation (Shanghai Chenhua). The three-electrode system was used in the testing process, and the prepared rGO/GCE, $CuO@Cu_2O$/GCE, $CuO@Cu_2O$/rGO/GCE, $CuO@Cu_2O$/NrGO/GCE and $CuO@Cu_2O$/PNrGO/GCE were used as the working electrode, the Ag/AgCl and Pt wire electrode were used as the reference electrode, and auxiliary electrode, respectively. i–t curves were measured at 0.6 V in 0.1 M NaOH solution for detection of glucose concentration. CV tests were performed over a potential range of 0–0.8 V (vs. Ag/AgCl) with a scan rate of 50 mV s^{-1}.

QUANTIFICATION AND STATISTICAL ANALYSIS

This study does not include statistical analysis or quantification.

ADDITIONAL RESOURCES

This study has not generated or contributed to a new website/forum and it is not part of a clinical trial.